Atmospheric Research 229 (2019) 240–254

Contents lists available at ScienceDirect

Atmospheric Research

journal homepage: www.elsevier.com/locate/atmosres

Investigation of sea-breeze/foehn in the Dead Sea valley employing high resolution WRF and observations

Pavel Kunin[a,*], Pinhas Alpert[a], Dorita Rostkier-Edelstein[b]

[a] The School of Geosciences, Department of Geophysics, Tel Aviv University, Tel Aviv, Israel
[b] Department of Applied Mathematics, The Environmental Sciences Division, Israel Institute for Biological Research, Ness-Ziona, Israel

ARTICLE INFO

Keywords:
Dead Sea
WRF Model
KITCube
Mediterranean Sea Breeze
Foehn
Lidar

ABSTRACT

The penetration of the uniquely strong Mediterranean Sea Breeze (MSB) into the Dead Sea (DS) valley has been studied for decades. However, the studies relied mostly on surface observations and coarse-model simulations. Motivated by the significant interdaily variability, we investigate two typical but different events: a frequent event in which the surface specific humidity (SH) steeply decreases and surface temperature increases during MSB penetration by ~40% and 1.2 °C, respectively; and a less frequent event, with almost the opposite behavior, an increase of surface SH by ~20%. Decrease in the integrated water vapor (IWV) content at MSB arrival is significantly larger in the first event. To reveal the factors responsible for these different behaviors we use high-resolution in–situ and remote-sensing observations, together with WRF simulations. It was found that foehn developed following the MSB descent down to the DS valley. The foehn characteristics were influenced by the synoptic and mesoscale conditions. While on the first event the foehn reached the surface of the valley, on the second it did not. This led to the different behavior of the surface temperature and SH. An additional factor was the amount of moisture brought by the DS breeze and MSB. Different altitudes of stable layers led to the different changes of the IWV. Our simulations suggest the feasibility of forecasting foehn and sudden changes in surface variables in the DS valley 24 h in advance. These forecasts can be most valuable during high pollution events.

1. Introduction

The Dead Sea (DS) valley is unique in the world because it is the lowest place on land (430 below MSL) with a very saline water body (DS) in its center. It is important to study the atmospheric circulation and be able to forecast the extreme weather conditions because of their influence on the population and the ecological system in the area. During the summer the DS valley weather conditions are dominated by a complex combination of synoptic, mesoscale, and local circulation patterns.

The summer climate in Israel is dominated by two main synoptic systems: the Persian Trough, an extension of a low-pressure system over the Persian Gulf reaching the Eastern Mediterranean region, and a high pressure system, an extension of the Azorean high (Alpert et al., 1990). They lead to prevailing westerly-northwesterly winds, known as the etesian winds (Ziv et al., 2004). Daily differences in the intensity of these synoptic systems lead to daily differences in wind speed and direction (Dayan et al., 2002; Berkovic, 2016).

In the mesoscale, the summer Israel climate is strongly affected by the Mediterranean Sea breeze (MSB, Alpert et al., 1982). The sea breeze (SB) is caused by the response to the daytime land-sea differential heating, creating a horizontal pressure gradient, thus enabling cool and humid marine air to penetrate inland. The SB is also modified by other parameters, i.e., the synoptic winds, atmospheric stability, and local topography features (Atkinson, 1981; Simpson, 1994; Alpert and Rabinovich-Hadar, 2003; Miller et al., 2003; Crosman and Horel, 2010). The summer synoptic flow in Israel creates weak large-scale forcing, providing favorable conditions for SB (Klai'c et al., 2009).

The climate of the DS valley is very hot and dry. It is an arid zone having large differences in the diurnal temperature and humidity cycles, while the weak lake breeze of the DS slightly tempers the hot and dry climate (Shafir and Alpert, 2011). The DS valley winds are dominated by a very high index of mesoscale activity even during the winter (Alpert and Eppel, 1985), showing that the local winds are dominant compared to the large-scale (synoptic) wind component throughout the year. The two main features in the daily wind cycle are the local DS breeze and the MSB (Ashbel, 1939; Bitan, 1977; Segal et al., 1983; Alpert, 1988; Lensky and Dayan, 2012; Naor et al., 2017). During the morning hours the DS breeze speeds up to 3–4 m/s in the NE direction at the southern DS coast. During the day the MSB flows up the Judean

---

* Corresponding author.
E-mail address: pavel.kunin@gmail.com (P. Kunin).

https://doi.org/10.1016/j.atmosres.2019.06.012
Received 25 December 2018; Received in revised form 21 May 2019

Mountains. The advance of the MSB on the Judean Mountains lacks some of the frontal characteristics such as the return current. Skibin and Hod (1979) suggest two reasons for it. The first is the domination of the steady etesian winds which mitigate perturbations in the breeze circulation advancement. The second is the moderate topography of the mountain range which reduces the inland thermal sea-land gradient.

After the MSB arrives at the top of the Judean Mountains it drops into the DS valley in the early evening hours (Segal et al., 1983; Naor et al., 2017) usually from the north-west (Bitan, 1977). Hence, this flow descends about 1200 m from the top of the Judean Mountains lee (~800 m above MSL) to the DS valley (430 m below MSL). Naor et al. (2017) performed an observational study of the MSB penetration into the DS region along an N-S cross-section that follows the Jordan and the Arava Valleys (located north and south, to the DS, respectively, Fig. 2). They adopted the Alpert and Rabinovich-Hadar (2003) method employing 4–5 criteria to define the exact time of the MSB penetration. They found that the average SB front (SBF) increases the local surface specific humidity (SH) as it reaches the DS valley along with significant temperature increases. However, analysis of recent measurements (Paperman, 2017), reveals that during most of the days (85%) the surface SH decreases while temperature increases (74%) at the MSB arrival time. In addition, change in wind direction from N-NE to NW and an increase of the wind speed follows the MSB arrival, too. In addition, it was earlier found that the MSB carries along coastal Mediterranean anthropogenic pollutants into the DS valley (Levin et al., 2005; Sever et al., 2017). Vüllers et al. (2018) reported that the significant descent of the MSB warms and dries the DS valley, giving rise to a foehn effect.

Foehn is a generic term for strong downslope winds with high temperature and low humidity on the lee side of a mountain ridge. Foehn winds occur downstream of most major mountain ridges in the world (Nkemdirim and Leggat, 1978; Richner and Hachler, 2013; Takane and Kusaka, 2011; Norte, 2015). Foehn characteristics include an increase in the wind speed and temperature and a decrease in relative humidity (Richner and Hachler, 2013). Kishcha et al. (2017) showed that foehn can occur in the DS valley as a result of a low-pressure system in the spring, too.

2. Objectives and events

The main objective here is to investigate the atmospheric phenomena in the DS valley during two events characterized by very different temperature and moisture behavior at the surface at the time of the MSB arrival. To this aim we analyze the synoptic, mesoscale and local scale atmospheric evolution in the DS during these events. Special attention is given to the MSB structure including the evolution of its depth, moisture, temperature and wind at the arrival time in the Judean Mountains and the DS valley. We combine two sophisticated tools: (1) unique very high-resolution (HR, both vertical and temporal) observations first conducted in the DS area and (2) HR Advanced Research Weather version of the Weather Forecast and Research mesoscale model (WRF hereafter, Skamarock et al., 2008) simulations. A primary challenge is to evaluate the WRF skill in simulating the HR MSB structure and the differences between the two case-studies, despite the known limitations of mesoscale models, particularly over highly complex terrain (e.g., Arnold et al., 2012). A few numerical studies (Doron and Neumann, 1977; Alpert et al., 1982; Segal et al., 1983) have attempted to simulate the MSB penetration into the Jordan valley, however, these earlier studies were relatively coarse and lacked the advanced HR observations.

The present study focuses on two days, 16 August 2014, when a strong sharp decrease of surface SH and a temperature increase were measured with the MSB arrival at the observed location (Fig. 1, Opera Area). The second event on the 8 August 2014, in which the surface SH increased and the surface temperature decreased. Fig. 4c, d show the quite different observed surface SH time-series for the two events along with the surface horizontal wind vector. The arrow on the horizontal axes indicates the time of dramatic change associated with MSB/foehn penetration, as will be shown later.

3. Methods

3.1. Measurements

In order to analyze the inland penetration of the MSB up to the Judean Mountains and DS valley as well as the potential foehn effect, we have analyzed observations from three meteorological surface stations located in the vicinity of the path followed by the MSB (see Fig. 2b and Table 1). The first station, Ashkelon (“A” in Fig. 2b), is located by the sea shore on the perpendicular line from the coast to the DS measurements site (red circle in Fig. 2b). The second one, Rosh Zurim (“R” in Fig. 2b), is located near the top of the ridge. The third, Maale Adumim (“M” in Fig. 2b), is located on the downwind/lee side. The stations are operated by the Israel Meteorological Service (IMS). The dataset included 10 min standard meteorological parameters such as air temperature, relative humidity, wind speed and direction. The time of MSB penetration at each station was found using the following criteria based on the Alpert and Rabinovich-Hadar (AR hereafter, Alpert and Rabinovich-Hadar, 2003) method. Notice that some minor modifications to AR were done due to different time resolution of the dataset:

- Wind direction: End of clockwise rotation (CWR) of at least 45^0 within 20 min (15 min in AR). If such a turning was not found, then the largest CWR that extended for at least 20 min (15 min in AR) was used.
- Wind speed: Beginning of a continuous wind increase of at least 1.5 m/s within 30 min (35 min in AR). If such a temporal gradient was not found, then the largest increase that extended for at least 30 min (25 min in AR) was used.
- Temperature: Beginning of a decrease or stabilization for at least 20 min (15 min in AR).
- Relative humidity: Beginning of an increase or stabilization for at least 20 min (15 min in AR).
- Turbulence intensity (gustiness). Point of maximum turbulence intensity.

Turbulence intensity may be defined as the ratio between the wind speed standard deviation and the average wind and calculated at each time based on the seven-point measurements (equivalent to 1 h time period) around the pertinent time.

The measurements at the DS valley were conducted as part of the Virtual Institute DEad SEa Research Venue (DESERVE) project using the KITcube instruments along with the Energy Balance Station (EBS). DESERVE was designed as a cross-disciplinary and cooperative international project of the Helmholtz Centers KIT, GFZ, and UFZ, with partners of the riparian countries (http://www.deserve-vi.net/). Long term meteorological background measurements (Energy Balance Stations, EBS hereafter), starting in 2006, combined with data from sophisticated remote sensing and scanning instruments deployed during special observation periods of about 2 months duration, August and November 2014, were conducted. These measurements provided 3D-winds, temperature, humidity, pressure, radiation, and visibility data at high temporal and vertical resolution. The observations were performed at the Masada foothills at the Opera area (Fig. 1). Soundings were launched to measure in-situ vertical profiles of meteorological data during Intensive Observational Periods at a time resolution of up to one hour. On 16 August 2014 12 radiosondes were launched (every 2 h, starting at 0100 UTC), and 6 on 8 of August 2014 (every 2 h, starting at 1300 UTC). Table 2 summarizes the list of instruments parameters used in the study.

Fig. 1. Google Earth's image of the terrain focused on the measurements site of the Opera Area at the MASADA foothills −350 m MSL. For the full geographical area, see Fig. 2.

3.2. Description of the instruments at the Opera area

A ground-based microwave radiometer designed by Radiometer Physics measures the sky brightness temperature at 12 frequencies distributed within the 22–30 GHz and 51–59 GHz bands. With statistical retrievals provided by U. Löhnert from the University of Cologne (Löhnert and Crewell, 2003; Crewell and Löhnert, 2003), these sky brightness temperatures are inverted to obtain temperature and humidity profiles up to 10 km height AGL and integrated water vapor (IWV) data along the line of sight. A 2 μm heterodyne wind lidar with beam width of 75 mm at laser exit (WindTracer, Lockheed Martin) measures aerosol backscatter and calculates radial velocity (Träumner et al., 2011). The lidar has two-axis scanners and yield profiles of the horizontal wind velocity via the velocity-azimuth display (VAD) technique (e.g., Browning and Wexler, 1968).

To cover the range between the surface and the lowest WindTracer measurement heights, a second wind lidar (Windcube 8, Leosphere) with a wavelength of 1.54 μm is used, which measures the wind profile from 40 m AGL up to about 600 m AGL with a time resolution of 7 s and a vertical range resolution of 20 m (Kalthoff et al., 2013).

To record the incoming radiance energy at the earth surface the EBS stations are used. These stations measure the components of the radiance balance, the sensible and latent heat flux as well as the soil heat flux. The stations measure also 3D wind components, temperature and moisture. Description of all EBS instruments can be found at https://www.imk-tro.kit.edu/english/2347.php/.

3.3. Model

3.3.1. Model description

For insight into the processes within the atmosphere with respect to time and space, model calculations are essential, as observations are normally limited to single points in space. We used the WRF model to analyze and better understand the complex processes in and around the DS area, e.g., the MSB structure and its propagation into the DS Valley.

The WRF model solves the compressible non-hydrostatic atmospheric equations in flux form on a mass-based, terrain-following, vertical coordinate system. HR global datasets are used to define the model topography and other static surface fields. For a complete description of the WRF modeling system, see, e.g., Skamarock et al. (2008). The WRF model has a nesting grid capability that allows zooming into a sub-region with high horizontal resolution by generating a series of higher resolution nested grids within the coarser parent grids. In addition, WRF includes a complete suite of physics schemes that account for the important atmospheric and land-surface physical processes. Several different formulations are available for each of them, thus, many combinations of model physics are possible. The model has been used for studying the influence of the SB in various regions (see e.g. Papanastasiou et al., 2010; Salvador et al., 2016). Employing the WRF model, Hu et al. (2010) and Arnold et al. (2012) emphasized the importance of using high vertical and horizontal resolution to capture Planetary Boundary Layer (PBL) processes, such as density currents. The SB behavior as a density current, and its onshore penetration, has been investigated using WRF model in several studies (Chemel and Sokhi, 2012; Robinson et al., 2013; Peace et al., 2015). Udina et al. (2013) and Soler et al. (2014) used both WRF and observations to investigate various aspects of density current over Northern Spain in the mountain area. These studies showed, in both model simulations and observations, that the arrival of the density currents is characterized by a sharp change in temperature, wind velocity, wind direction, and specific humidity.

3.3.2. Model setup

A pre-requisite for relying on model simulations to analyze atmospheric processes is to verify their skill with respect to observations. Therefore, a significant effort was made to find a favorable WRF model configuration. Some WRF parameters and parameterizations were chosen based on modeling studies over complex terrain (e.g. Zhang et al., 2013; Miao et al., 2015; Hari Prasad et al., 2017), others were chosen after running sensitivity tests and comparing model results to observations.

WRF 3.5.1 version was configured with four nested domains with

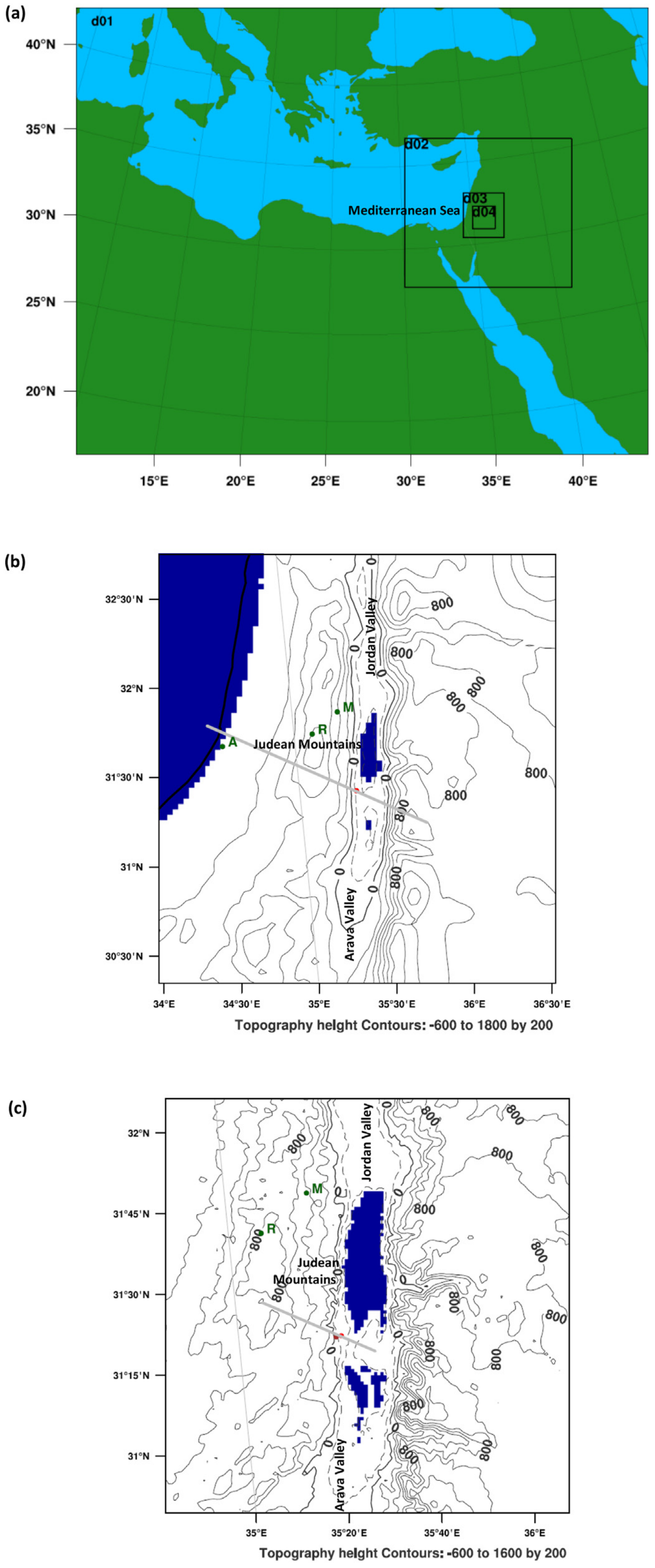

Fig. 2. The four WRF-model nested domains configuration over the Eastern Mediterranean region (a). The model domains are: d01, d02, d03 and d04 with horizontal resolutions of 30, 10, 3.3 and 1.1 km grid size, respectively. The inner domains d03 (b) and d04 (c), focused on the DS area, are shown in detail. Red and brown circles denote the Masada measurements site and the Masada Top, respectively. Green circles are meteorological surface stations. Topography contours in the lower panel are drawn at 200 m intervals. Dashed lines represent topography below mean sea level. The DS and Mediterranean Sea are denoted in blue. The grey lines in (b) and (c) are the cross-section lines for Fig. 3 and Fig. 11, respectively. (For interpretation of the references to colour in this figure legend, the reader is referred to the web version of this article.)

Table 1
Location and altitude of three meteorological stations used for MSB confirmation (a), time of MSB arrival according to the 5 parameters method (Alpert and Rabinovich-Hadar, 2003) at Ashkelon (b), Rosh Zurim (c) and Maale Adumim (d). WD – wind direction, WS – wind speed, T- temperature, RH – relative humidity, G – gustiness, X – no time that fits the criteria was found.

a)

Station	Location	Altitude (m)
Ashkelon	31.64 N, 34.52E	5
Rosh Zurim	31.66 N, 35.12E	950
Maale Adumim	31.77 N, 35.30E	490

b)

Ashkelon	8 August 2014	16 August 2014
Parameter	Time (UTC)	Time (UTC)
WD	05:50	05:30
WS	06:20	06:00
T	05:40	06:40
RH	X	X
G	05:20	05:50

c)

Rosh Zurim	8 August 2014	16 August 2014
Parameter	Time (UTC)	Time (UTC)
WD	11:00	10:20
WS	10:00	09:20
T	11:00	10:40
RH	10:50	10:30
G	09:40	09:20

d)

Maale Adumim	8 August 2014	16 August 2014
Parameter	Time (UTC)	Time (UTC)
WD	11:10	11:10
WS	11:10	10:40
T	11:10	11:30
RH	11:30	11:40
G	11:10	10:20

30, 10, 3.3 and 1.1 km grid spacing (Fig. 2a).

The Monin–Obukhov scheme (Janjic, 1996 and Janjic, 2002) and the Lin et al. (1983) scheme were used to simulate surface layer physics and atmospheric microphysics, respectively. The Grell 3D ensemble scheme (Grell, 1993 and Grell and Devenyi, 2002) was used by the model to parameterize cumulus physics in the two coarser domains. The RRTMG scheme (Iacono et al., 2008) was used to simulate long and short wave radiation fluxes. The Unified Noah Land Surface Model (Tewari et al., 2004) was used to account for soil dynamics. Second order diffusion in coordinate surfaces was used for turbulence and mixing and horizontal Smagorinsky first order closure (Smagorinsky, 1963).The model sensitivity was checked for: (1) landuse/vegetation database [(a) USGS 30 s, (b) MODIS 30s and (c) MODIS 15 s resolution], (2) PBL schemes [(a) The Mellor–Yamada–Janjic (MYJ) TKE scheme

Table 2
A list of the instruments and measured parameters that were used in the study.

Instrument	Measured/derived variables
EBS and IMS stations	10 m horizontal winds, 2 m SH and temperature
Windcube lidar	Profiles of horizontal and vertical winds
Windtracer lidar	Profiles of horizontal winds
Radiosondes	Profiles of horizontal winds, temperature, relative humidity and pressure
Radiometer	Integrated water vapor

(Janjic, 1994) and (b) the Yonsei University (YSU) first-order closure non-local scheme (Hong et al., 2006)], (3) number of vertical levels [(a) 32, (b) 40], (4) atmospheric and soil initial and lateral boundary conditions from global models (IC/BC) [(a) NCEP's Global Analysis (GFS) at a horizontal resolution of 0.5^0 (http://rda.ucar.edu/datasets/ds335.0/#access), (b) ECMWF operational analysis and forecasts at horizontal resolution of 15 km (https://www.ecmwf.int/en/forecasts/documentation-and-support, using 3 nested domains only with grid size 10, 3.3 and 1.1 km) (c) NCEP for soil and ECMWF for atmosphere IC/BC], (5) initial conditions for the finest domain from [(a) global model, (b) parent domain], (6) initialization time of coarse domains [(a)15 August 2014 00 UTC, (b)16 August 2014 00 UTC, (7) initialization time of finest domain [(a) same as coarse domains, (b) later]. The sensitivity tests were run only for the 16 August event because not all instruments were available for the 8 August event to allow comparison with the model. Table 3 summarizes the 11 simulations that were run to determine the best model configuration for the study. Evaluation against observations was made for seven parameters: surface SH, surface temperature, surface wind, vertically integrated water vapor (IWV), time evolution of horizontal-wind profile, time evolution of vertical-wind profile and time of MSB arrival at the DS valley. For each parameter and simulation a score was assigned between 1 and 4 (4 states the best agreement between model and observations, Table A.1). Two configurations achieved the same highest score, simulation 5 and simulation 9. Our sensitivity runs show that shorter spin-up times for the fine domain were sufficient to develop the *meso* and local scale dynamics that are strongly forced by the high resolution very complex terrain and sea-land contrast. Longer spin-up times for the fine domain resulted in unskilled simulations as a result of error growth. The use of higher resolution ECMWF model for initial and boundary conditions resulted in poor skill while the coarser NCEP/GFS model led to more skilled simulations. We note that NCEP/GFS shares same land-surface model and other parameterizations with WRF, thus leading to more balanced initialization.

We chose configuration number 5 as it showed better agreement (than configuration number 9) with the observations of surface temperature and SH, the motivation for this study, as shown in Fig. 4 (detailed discussion is presented in Section 3.1).

The following choices, based on the aforementioned sensitivity tests, complete the most suitable WRF configuration used in our study: 40 vertical levels up to 50 hPa with 20 of them within the lowest 1.5 km above the surface (which ensures high vertical resolution at heights where the SB density current develops), landuse/vegetation provided by MODIS dataset with a 15 s resolution and GFS IC/BC for the atmosphere and soil. The three coarser domains were initialized on the 15 August and 7 August 0000 UTC, for the 16 and 8 August events, respectively, to allow for model spin up. The finest domain was initialized 24 h later to diminish error growth from the lateral boundaries. Due to the complex terrain that strongly forces the PBL dynamics, the spin-up time for the finest domain is short (~3 h).

Details on the comparison between the selected model configuration and the observations are presented in Section 4, illustrating the evaluation procedure that was applied to the set of 11 sensitivity tests.

4. Results

Next, the synoptic flow, the MSB/foehn development including the MSB inland penetration up to the Judean Mountains and down to the DS valley, as well as the DS valley atmospheric circulation during the two events, are investigated. First, the observations are analyzed and then compared to the model. By doing so we assess the model skill to analyze the selected events using additional 3D model fields.

We note that in spite of the HR 1.1 km grid, it is quite challenging to obtain a very accurate representation of some complex terrain features (Fig. 1 and Fig. 2). Thus, discrepancies between model and observations may be expected. For instance, the Masada Mountain, a terrain feature that affects the local circulation located west to the measurements site (Fig. 1), is not well represented by the 1.1 km grid. Another significant approximation when running the WRF model over complex terrain is the use of the Monin–Obukhov scheme and the 1D PBL parameterization which is developed primarily for flat terrain. Despite these limitations, the model seems to perform well in simulating the 3D atmospheric evolution as well as in reproducing the differences between the two events, as shown below.

4.1. MSB development and inland penetration

The event of 16 August was under one of the typical summer synoptic systems called Persian Trough (following Alpert et al., 2004, see Appendix A and Supplementary Fig. S1). The MSB developed at the coast between 0530 and 0640 UTC (Ashkelon station, Table 1b, LT = UTC + 3). At 0930 (hereafter in UTC) the MSB reached the top of the mountain (Rosh Zurim station, Table 1c). Between 1100 and 1130 it passed the station located on the downwind side (Maale Adumim station, Table 1d).

During 8 August the Israel area was influenced by the High to West (High pressure system with its pressure-center located west to Israel, Alpert et al., 2004, see Appendix A and Supplementary Fig. S2). Similarly, the MSB developed at the coast between 0540 and 0620 UTC

Table 3
Description of the sensitivity simulations.

Simulation number	Landuse	PBL	Number of vertical levels	IC/BC of coarse domain	IC/BC of finest domain	Initial time of coarse domains (DD/MM hh)	Initial time of finest domain (DD/MM hh)	Score
1	USGS	MYJ	32	GFS	GFS	15/08 00	15/08 00	15
2	MODIS 30 s	MYJ	32	GFS	GFS	15/08 00	15/08 00	10
3	MODIS 15 s	MYJ	32	GFS	GFS	15/08 00	15/08 00	15
4	MODIS 15 s	MYJ	40	GFS	GFS	15/08 00	15/08 00	15
5	MODIS 15 s	MYJ	40	GFS	GFS	15/08 00	16/08 00	22
6	MODIS 15 s	MYJ	40	GFS	GFS	15/08 00	15/08 12	21
7	MODIS 15 s	YSU	40	GFS	GFS	15/08 00	16/08 00	8
8	MODIS 15 s	MYJ	40	GFS	GFS	16/08 00	16/08 00	21
9	MODIS 15 s	MYJ	40	GFS	Parent domain	15/08 00	16/08 00	22
10	MODIS 15 s	MYJ	40	ECMWF	ECMWF	15/08 00	16/08 00	13
11	MODIS 15 s	MYJ	40	ECMWF/GFS	ECMWF/GFS	15/08 00	16/08 00	13

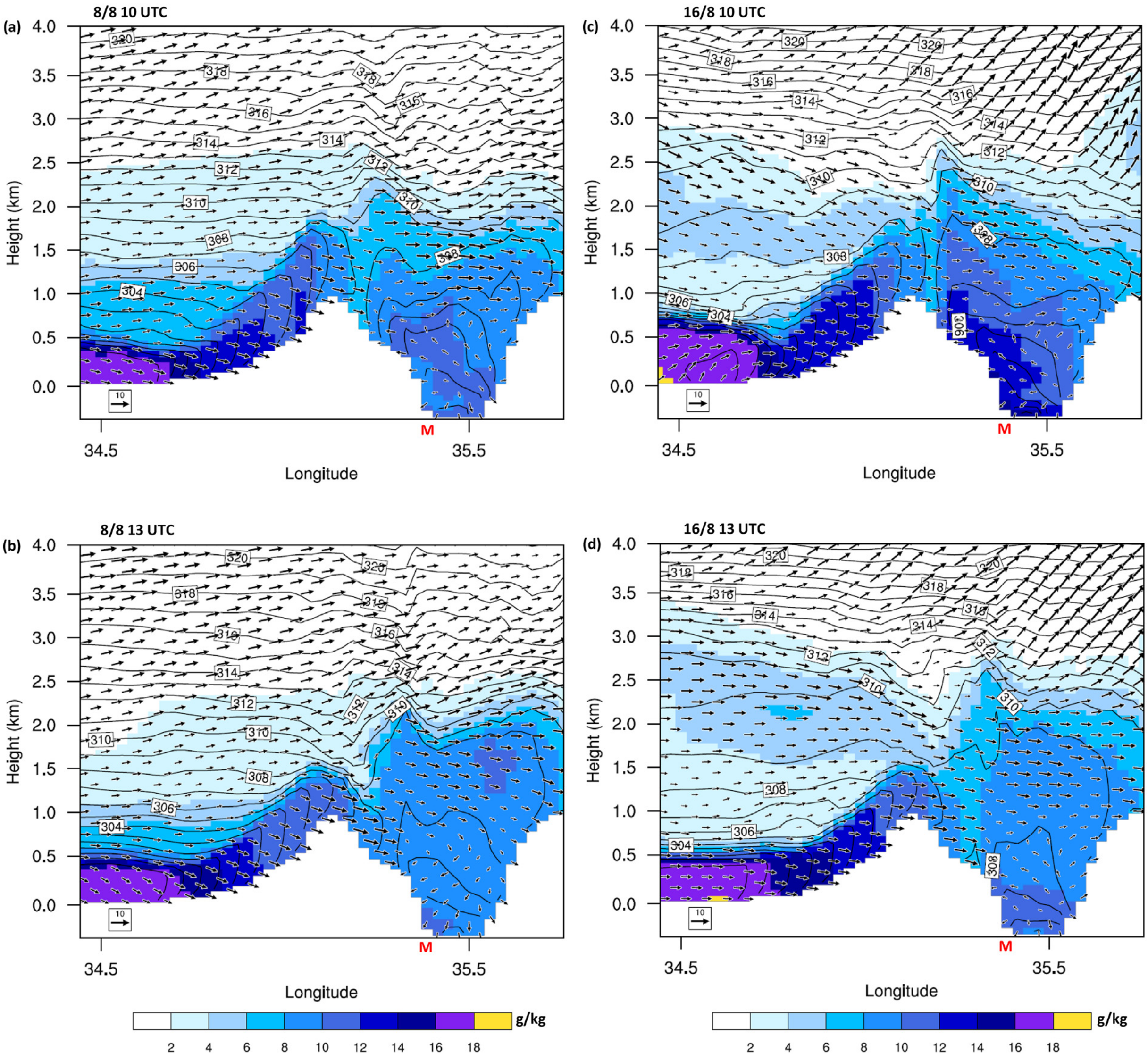

Fig. 3. WRF model perpendicular to the coast cross-sections from 3.3 grid spacing resolution domain (d03, Fig. 2a) for 2 chosen times (a) 1000 and (b) 1300 UTC on 8 August 2014; (c) 1000 and (d) 1300 UTC on 16 August 2014. Shaded colors represent specific humidity (g/kg, colour bar at the bottom), black contours potential temperature (K) and vectors for horizontal winds. "M" at the horizontal axis indicates the location of the Opera measurements area.

(Table 2b). At 1100 and 1110 it reached the top of the mountain and the station located downwind side, respectively (Table 2c and d). The differences in the times of MSB arrival between the two mountain stations result from their different locations and different synoptic conditions on the two days. The stations are not on the same paths of MSB penetration. To reach the Rosh Zurim station the MSB climbs about 1 km, but to reach the Maale Adumim station, the MSB climbs only 600 m and then descends 200 m. The second reason is the synoptic differences between the two days. On 8 August the lower inversion (the Bet-Dagan near-coastal radiosonde at 12 UTC reported 450 m vs. 750 m on 16 August) associated with the high pressure system reduces wind speed of the MSB as it climbs toward the Rosh Zurim station.

The model simulated well the inland penetration of the MSB on both days as seen in the cross sections perpendicular to the coast reaching the Masada site (Fig. 3, see Fig. 2b for the cross section line). The model potential temperature, specific humidity and horizontal winds, show that the MSB reaches the top of the mountain at 10 UTC (Fig. 3a, c), corresponding to the mountain stations observations (Table 1), on both days. The modeled MSB may be identified by its front denoted by the potential temperature isopleths and the specific humidity that follows these isopleths (Simpson et al., 1977). The model MSB had westerly winds on 16 August (Fig. 3c,d) and west-northwest winds on 8 August (Fig. 3a,b, similar to the observations at Rosh Zurim station, not shown here). The vertical depth of the model MSB on both days is about 1 km. At the time of model MSB arrival at the top of the mountain, the model DS breeze superposed with anabatic winds (located on the eastern slope) opposing the MSB descent (Fig. 3a,c). At 13 UTC (Fig. 3b,d) the model DS breeze weakens following the reduced solar heating and the model MSB starts its descent from top of the mountain to the DS Valley.

4.2. *Dead Sea valley atmospheric dynamics*

4.2.1. *Surface variables: SH, temperature and wind*

EBS surface measurements (at the Opera Area, Fig. 1) show that on the 16 of August the surface wind direction between 1300 and 1430 UTC was *E*-NE (Fig. 4a) due to the DS breeze, which brought moist air to the measurements site (Fig. 4c, the DS is located E to the measurements area, see Figs. 1, 2). Between 1430 and 1700 UTC the wind direction changed first to NW, and then gradually to W. At the same time the wind speed increased from 1 m/s before 1430 up to 8 m/s a few hours after. The surface SH steeply decreased by 40% and the surface temperature increased by 1.2 °C. The increase in the wind speed,

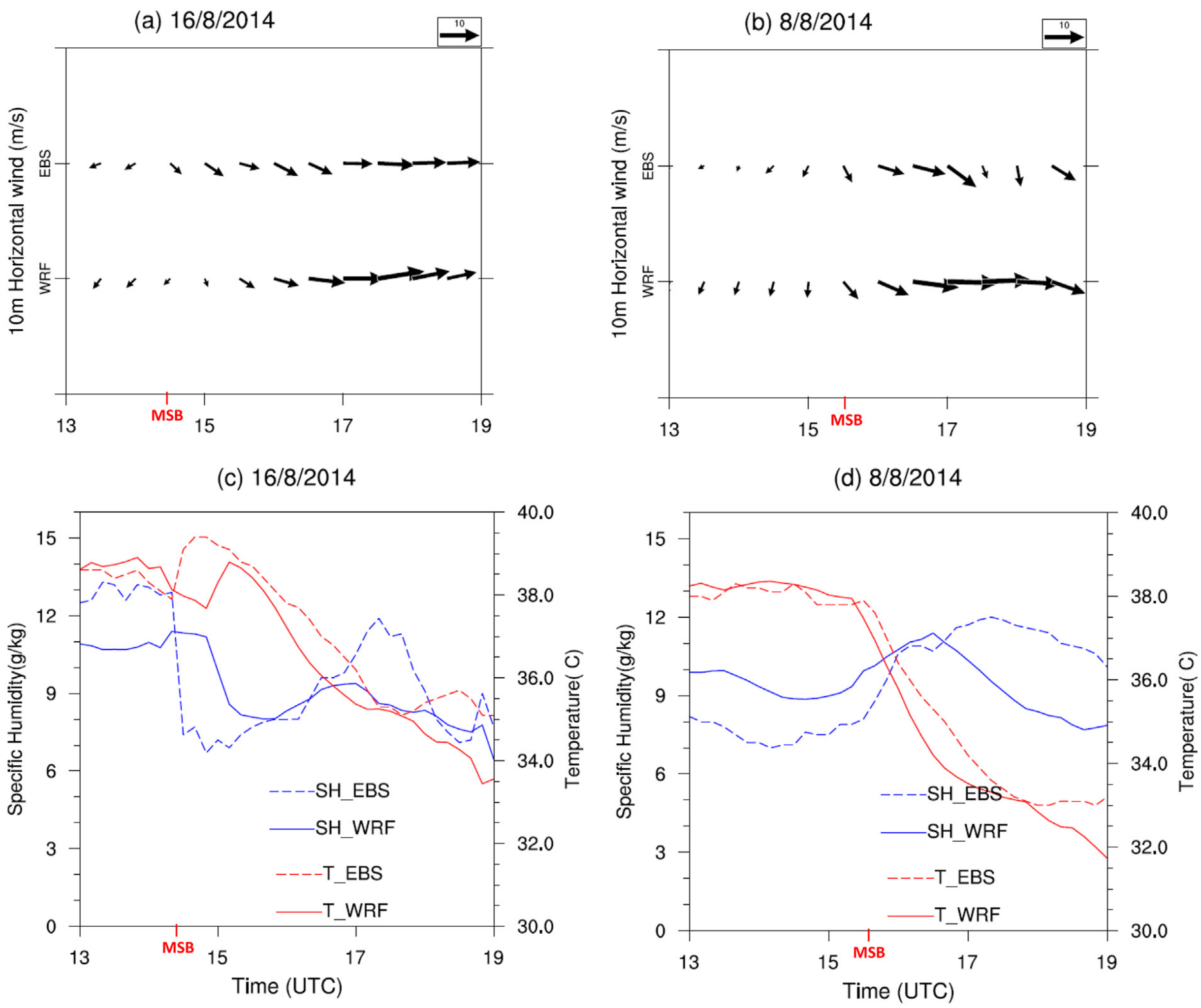

Fig. 4. Horizontal wind arrows at 10 m above ground level (AGL) for (a) 16 August and (b) 8 August 2014 from EBS measurements and WRF simulation (see Section 3). Specific humidity (blue line) and temperature (red line) at 2 m AGL for (c) 16 August and (d) 8 August 2014 from EBS measurements (dashed line) and WRF simulation (solid line). "MSB" at the horizontal axis indicates the MSB arrival time. Horizontal axis time (UTC); local time is given by UTC + 3. (For interpretation of the references to colour in this figure legend, the reader is referred to the web version of this article.)

change in wind direction to NW together with changes in surface SH and temperatures are all indicators of the MSB arrival, similar to observations by Naor et al., 2017 (see Section 1). This circulation dominated the valley flow until 1900 UTC and then it vanished. The model reproduced well the steep changes half an hour later than the observed. The decrease in surface SH was shallower in the simulation. This could be attributed to enhanced horizontal diffusion in the model (the sign of horizontal diffusion is opposite to the advection). Due to the steep topography the horizontal diffusion calculated by the model on the terrain following coordinate is not 'purely' horizontal and it is larger than it should be (Alpert and Neumann, 1984).

On the 8 of August EBS surface measurements show that the surface wind was very weak until 1520 UTC (Fig. 4b). The wind direction changed on this period between NE and N. Between 1520 and 1700 UTC the wind direction changed first to NW, and then gradually to W. The wind speed increased from 1 m/s up to 8 m/s. These steep changes are manifestations of the MSB arrival at the mountain range and the descent of the air mass into the DS valley, similar to 16 August. However, as opposed to the 16 August, the surface SH and temperature gradually increased by 20% and decreased by 2 °C in 40 min, respectively. The value of the surface SH before the MSB arrival was lower than on the 16 August (by ~5 g/kg) due to weaker and less easterly surface winds, which brought less moisture from the DS. The model captured well the influence of the MSB on the surface parameters for this day, too. Still, model-observations differences are noticed. Stronger model winds before the MSB arrival, and earlier arrival of the model MSB by half an hour.

In spite of the differences between the model and observations the model clearly shows the differences between both events and follows the observed time evolution.

In the next section we analyze the vertical profiles and relate them to the results obtained for the surface variables.

4.2.2. Vertical profiles

4.2.2.1. Horizontal and vertical wind profile analysis. On the 16 of August Windtracer observations (Fig. 5b) show that the MSB reaches the surface at 1430 UTC. Similarly to what we saw from the surface measurements (Fig. 4), the MSB arrival was accompanied by a surface wind direction change from NE to NW and an increase of wind speed up to ~10 m/s. This change in horizontal wind appears at all levels up to 1000 m AGL. At 1700 UTC the radiosonde (Fig. 5a) shows the SB front (SBF) nose at a height of 200–300 m AGL (as in a typical SBF described by Lin, 2007). The model (Fig. 5c) captured fairly well the large-scale flow at the upper levels (1200–2000 m AGL) and the SBF nose. In both, model and Windtracer observations, the effect of the MSB (wind-direction change and wind-speed increase) in the DS valley between 1500 and 1900 UTC, is well noticed. Still, as expected, some model-observations differences exist as follows.

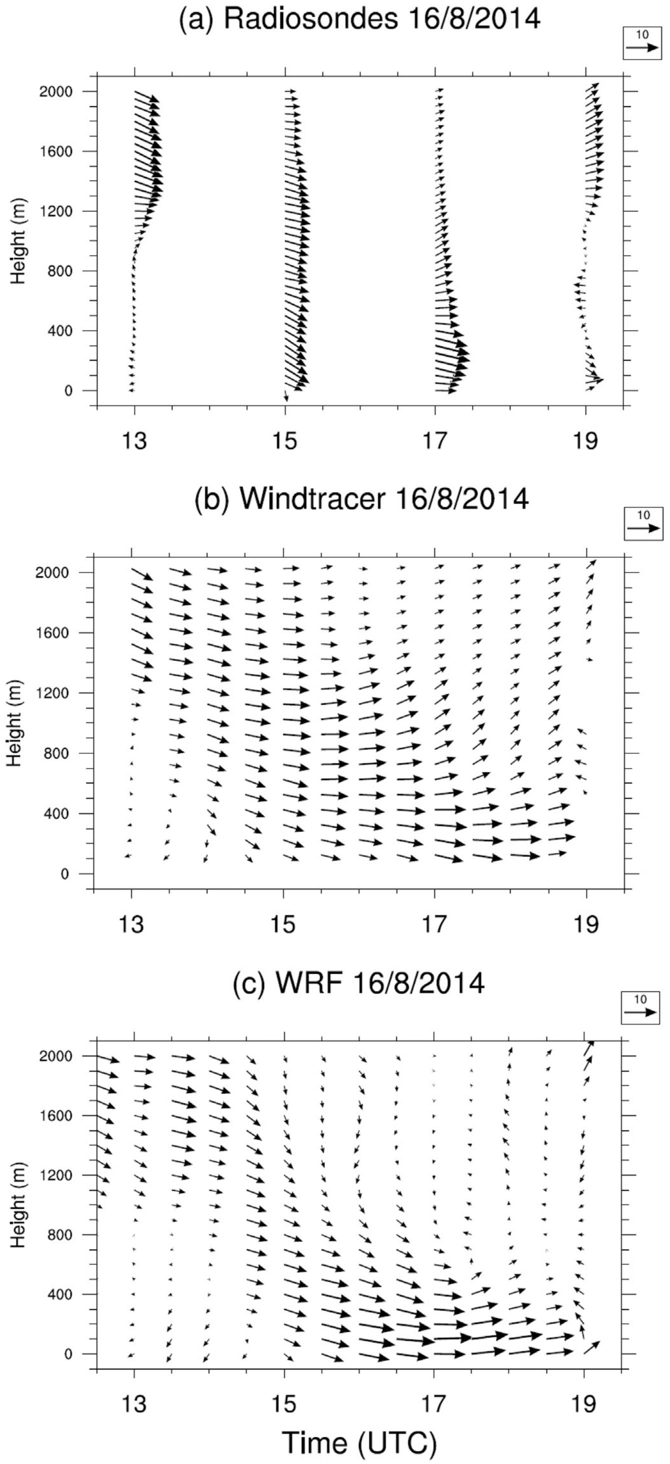
(a) Radiosondes 16/8/2014

(b) Windtracer 16/8/2014

(c) WRF 16/8/2014

Fig. 5. Horizontal wind (arrows) from (a) radiosondes at 2 h time intervals, (b) Windtracer at 0.5 h time intervals and (c) WRF model at 0.5 h time intervals for the 16 August 2014. Zero height refers to the ground level of the measurements (~ −350 m ASL; the Opera area, Fig. 1). Local time: UTC + 3. Wind scale (in m/s) is shown at the upper-right corner of each panel.

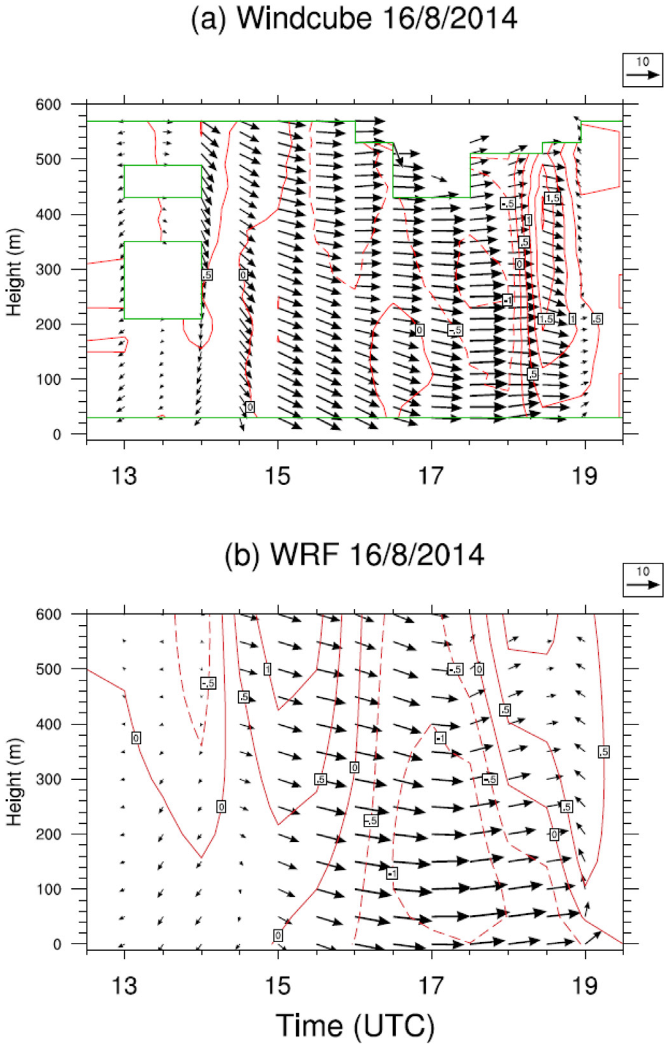
(a) Windcube 16/8/2014

(b) WRF 16/8/2014

Fig. 6. Horizontal (arrows) and vertical wind (contours) components from (a) Windcube and (b) WRF model at 0.5 h time intervals for the 16 August 2014. Zero height refers to the ground level of the measurements (~ −350 m ASL; the Opera area, Fig. 1). Local time is UTC + 3. Green boxes in (a) indicate missing values. Horizontal wind scale (in m/s) is shown at the upper-right corner of each panel. Vertical wind speed contours are drawn at 0.5 m/s intervals. Solid/dashed lines represent upward/downward vertical wind. (For interpretation of the references to colour in this figure legend, the reader is referred to the web version of this article.)

In both, Windcube observations and model (Fig. 6), downward vertical winds developed with the effect of the MSB descent. However, the simulated vertical velocity (between −0.5 and −1 m/s, Fig. 6b) was stronger than observed (which was weaker than −0.5 m/s, Fig. 6a) at 1600–1700 UTC. This is likely due to the smoother slope in the model than in the real terrain, which causes less loss of momentum. Before the MSB arrival the vertical velocity was close to zero in all analyzed vertical levels, both in model and Windcube observations. During the MSB domination period the vertical velocity became negative in all levels up to 2000 m AGL with a maximum of 1 m/s between 200 and 400 m AGL in the Windcube observations (between 1700 and 1800 UTC), and with a maximum of 1 m/s between 50 and 400 m AGL in the simulation (between 1630 and 1800 UTC).

On 8 August, data from the lidars were unavailable, thus the validation of the model winds along the vertical profile was made only with respect to radiosondes. Radiosondes (Fig. 7a) show that the MSB enters the valley after 15 UTC. As on 16 August, wind direction changed from NE to NW wind speed increased (up to ~10 m/s) followed the MSB arrival. The SBF nose is noticed at 100–200 m AGL. As opposed to 16 August, the change in horizontal wind occurred only in lower levels (up to 400 m AGL). Above 400 m, the horizontal wind speed was lower and wind direction slightly different. The observed MSB dominated the valley for less than four hours this time. The model captured well the synoptic flow (above 1200 m AGL), the MSB arrival time, its vertical depth, and the period of the MSB influence. Similarly to what we saw

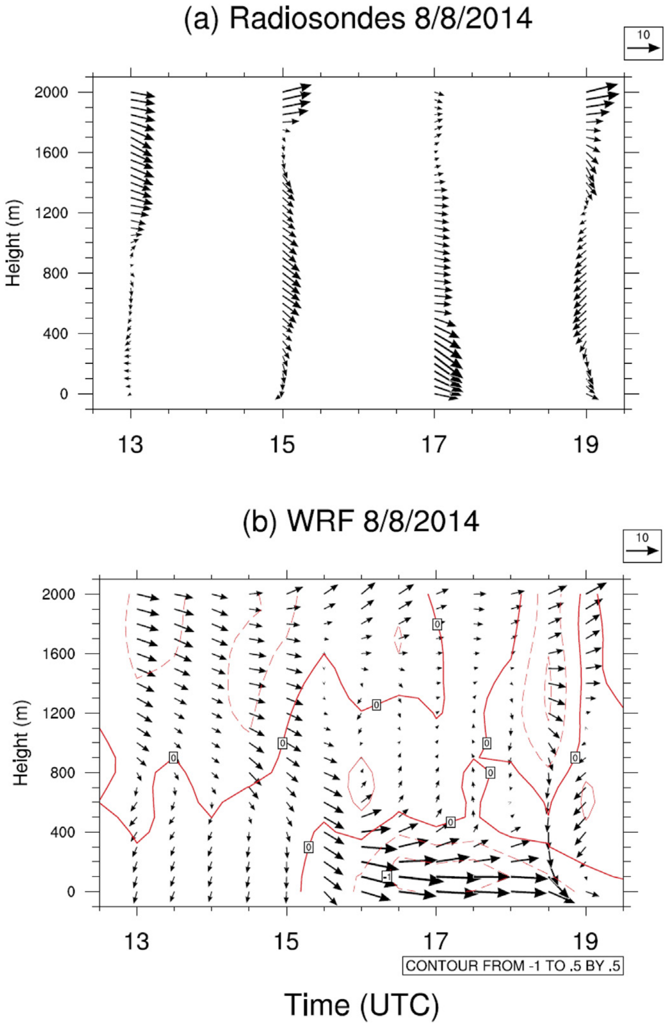

Fig. 7. Horizontal wind (arrows) from (a) radiosondes at 2 h time intervals, (b) WRF model at 0.5 h time intervals, for the 8 August 2014. Zero height refers to the ground level of the measurements (~ -350 m ASL; the Opera area, Fig. 1). Wind scale (in m/s) is shown at the upper-right corner of each panel.

from the EBS surface measurements (Fig. 4), the model MSB reached the surface of the DS valley at about 1530 UTC (Fig. 7). Downward vertical wind developed up to 400 m AGL.

Between 1300 and 1500 UTC a change in wind direction from NW to SW above 1800 m AGL (1400 above MSL) is observed, due to the displacement of the high pressure system that dominated the area on this day (Fig. S2).

The different vertical depths of the MSB on 8 and 16 of August are a result of the different synoptic conditions. Fig. 8 shows vertical profiles of potential temperature at 15 UTC on 8 and 16 August, measured by the radiosondes and simulated by the model (the modelled profile for 16 August is valid at 1510 UTC due later model MSB arrival). Although there are differences between the observed and model profiles, the model reproduces the differences between both days regarding the vertical location of unstable, neutral, and stable layers along the profile. We link the lower vertical extent of the MSB on 8 August with the lower inversion at about 400–500 m AGL, associated with the synoptic high pressure system that dominated the area. This inversion decouples the boundary layer from the free atmosphere and it is not present on 16 August dominated by a Weak Persian trough synoptic system.

4.2.2.2. Moisture profile analysis. Fig. 9a shows the behavior of the IWV during 16 August as measured by the radiometer and simulated by the model. Although in the simulation the MSB arrived half hour later, both the radiometer and the model, show the same temporal evolution with total decrease of almost half of its maximum value.

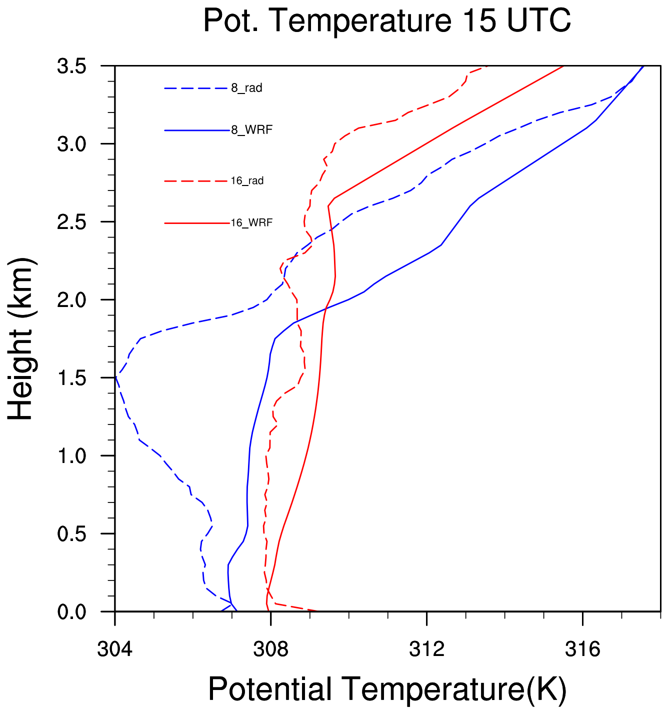

Fig. 8. Potential temperature profile at 15 UTC at 16 August (blue line) and 8 August (red line) from radiosonde (broken line) and WRF (solid line). Model potential temperature on 16 August is valid at 1510 UTC due to later model MSB arrival. (For interpretation of the references to colour in this figure legend, the reader is referred to the web version of this article.)

Since the radiometer only provides vertically integrated values of moisture, we rely on radiosondes and model simulations to analyze the evolution of the moisture and temperature in the various vertical levels (Fig. 10). The SH vertical profile is reasonably well simulated by the model. We can see in both radiosondes and model (Fig. 10a, b), a sharp decrease in SH along the atmosphere column at the time that the MSB enters the valley (1500 UTC, since radiosondes were launched every 2 h there is a smoother picture than in model profiles). Before the MSB arrival, model and radiosondes show that the air temperature is almost constant in time above 1 km AGL (above the mountain slope). They show that at lower levels the heating/cooling of the east-facing mountain slope influenced the air temperature: an increase until 1400 UTC and a decrease between 1400 and 1500 UTC (this hourly change cannot be seen in the radiosondes because of the coarse time resolution). At 1500 UTC, both radiosondes and model show that the air temperature up to 1 km AGL increased by 1 °C with the MSB arrival. Afterwards the temperature gradually decreased as expected from the mountain slope cooling.

During the 8 August the radiometer shows that the IWV also decreased with the MSB arrival (Fig. 9b) but the radiosondes and model show this time that the SH in lower levels (from the ground up to 400 m AGL) increased (Fig. 10c, d). The model simulated well both the increase of SH in the lower levels (0–400 m AGL, Fig. 10d) and the decrease of IWV (Fig. 9b). The temperature is almost the same between 1300 and 1530 on the lower levels (0–1000 m AGL). With the MSB arrival at 1530 the model temperature decreased between 0 and 400 m AGL and increased between 400 and 1000 m AGL. Similar temperature behavior is seen in the radiosondes but the exact time cannot be determined due to the coarse time resolution. The different behavior above and below 400 m AGL is associated with the inversion layer at 400–500 m as seen in Fig. 8. After the MSB arrival the temperature

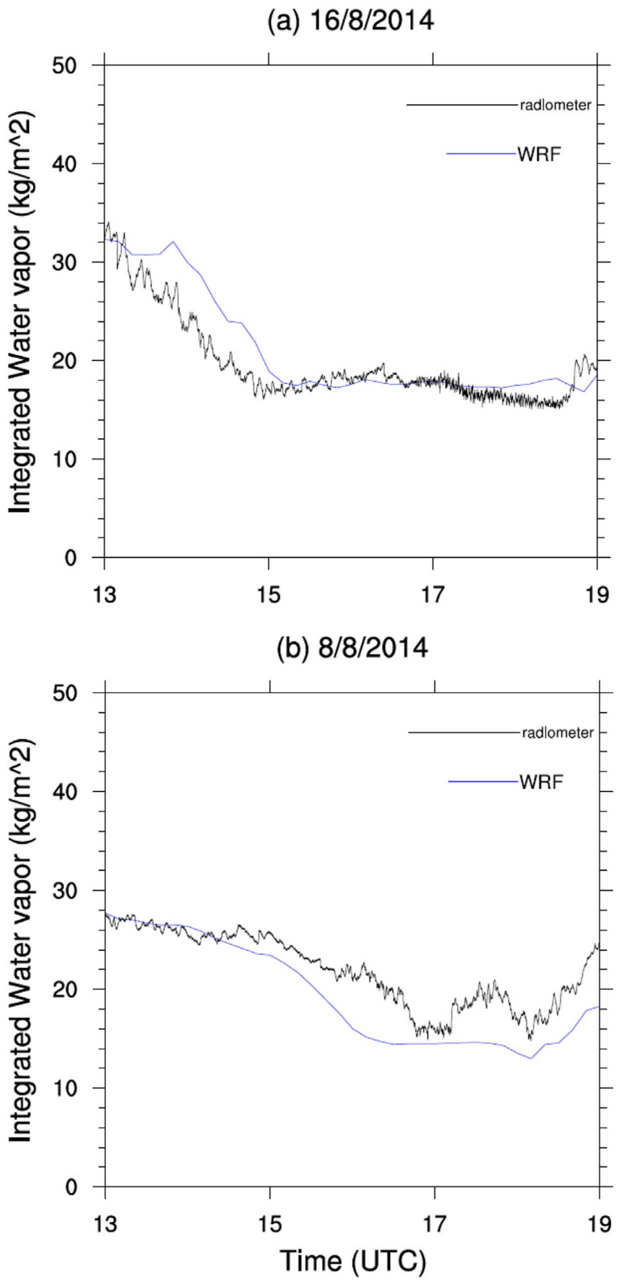

Fig. 9. Integrated water vapor (kg/m^2) from the radiometer (black line) and WRF model (blue line) for the (a) 16 August 2014 and (b) 8 August 2014. Local time: UTC + 3. (For interpretation of the references to colour in this figure legend, the reader is referred to the web version of this article.)

decreased at all levels, similar to 16 August, due to the mountain slope cooling.

The much higher decrease of IWV on the 16 August in comparison to that on the 8 is associated with the different location of the stable layer observed on the two days (Fig. 8). On 8 August, the stable layer, located above 1500 m AGL, prevents from the dry air above it from descending into the DS valley. On the 16 August the stable layer is located above 2500 m AGL. Descent of dry air (located above 1500 m AGL) with the MSB arrival caused an additional decrease of IWV. The air descent can be seen in the model cross sections (next section).

The drying, warming, change in wind direction and downward winds indicate that foehn phenomena developed here. On 16 August the foehn penetrated down to the surface, while on the 8 August it developed only between 400 and 1000 m AGL (the SH decrease and temperature increase with MSB arrival, see Fig. 10).

Section 4.2.3 further analyzes the factors responsible for the observed temperature/SH/winds behavior along the column using the model simulations.

4.2.3. Vertical model cross sections perpendicular to the coast

To further analyze the influence of the MSB on the DS valley, we take advantage of additional model information, which is not available in the observations. Model cross-sections of potential temperature, SH and wind streamlines are shown in Fig. 11. For 16 August (Fig. 11a, b), the difference in potential temperature and SH at the time of the MSB descent into the valley (1500 UTC) as compared to the time of MSB post-penetration in the valley (1600 UTC), is well noted. At 1600 UTC the boundary layer becomes drier and warmer (following the foehn effect) as the density current (see next) descended adiabatically from ~1200 m above MSL to ~400 m below MSL, i.e., the same potential temperature (307.5 K) is connecting the altitudes of the 1200 and −400 m and the streamline follows the isentropic line (Fig. 11b). The density current was identified following the calculation of differences between the air density above the mountain and that above the valley at the time of the MSB arrival (following Alpert et al., 1982 analysis, not shown here). We can see the enhancement of the MSB by the synoptic flow as the downward wind extends from 2 km above MSL down to the ground. As the flow reaches the DS valley surface it flows toward the DS eastern side.

In comparison, on 8 August (Fig. 11c, d), we can similarly see the drying between 1500 UTC and 1600 UTC but without reaching the ground as on 16 August. Two factors can be linked to these different outcomes on the two days: First, on 8 August, an inversion layer was located at ~400 m above the surface (at the measurement site, M in Fig. 11), while on 16 August the inversion layer was not present (Fig. 8 and Fig. 11). As a result of this layer stability on the 8 August, the increase of temperature is limited to heights 1000–400 m and alon not all the way to the ground as on the 16 August. There is even a temperature decrease noticed in the model simulations on 8 August below 400 m due to surface afternoon cooling (Fig. 10d). This temperature decrease is noticed to a lesser extent in the radiosondes, too (Fig. 10c). The second factor responsible for the differences between the two days is related to the contribution of the synoptic flow described as follows. On 8 August there is no enhancement of the downward motion by the synoptic flow because of an elevated stable layer extending from 1200 above MSL, as seen in Fig. 8 and Fig. 11c,d (the downward wind extends only from 1200 m above MSL toward the surface).

An hydraulic jump, a phenomenon that happens on the lee side of the mountain after a transition from subcritical to supercritical flow over the crest (Duran, 1990), is observed in the cross sections for both days by the rising isentropes east of the measurements site (M, Fig. 11). This was also confirmed in the 16 August observations, Vüllers et al. (2018). Table 4 presents the comparison of the dominant hydraulic jumps parameters noticed for both days. The Froude numbers (*Fr)* were calculated following Eq. (1).

$$Fr = \frac{u}{\sqrt{g'\eta}} \tag{1}$$

where u is the mean velocity of the lower layer (below the inversion base), η is the inversion base height, $g' = g\Delta\theta/\theta$ is the reduced gravity, Θ is the mean potential temperature of this layer and Δθ is the inversion strength.

The results in Table 4 support the aforementioned transitions that go along with the hydraulic jump on both days. The maximum vertical velocity is almost double on 16 August, which is in agreement with the extended downward motion on this day as well as the lack of the stable layer at 400–500 AGL (found on 8 Aug as described earlier, Fig. 8, Fig. 11).

Different spatial patterns of the SH, west of the measurements site (M, Fig. 11), are also observed on these two days. On 8 August the low

(a) Radiosondes 16/8/2014

(c) Radiosondes 8/8/2014

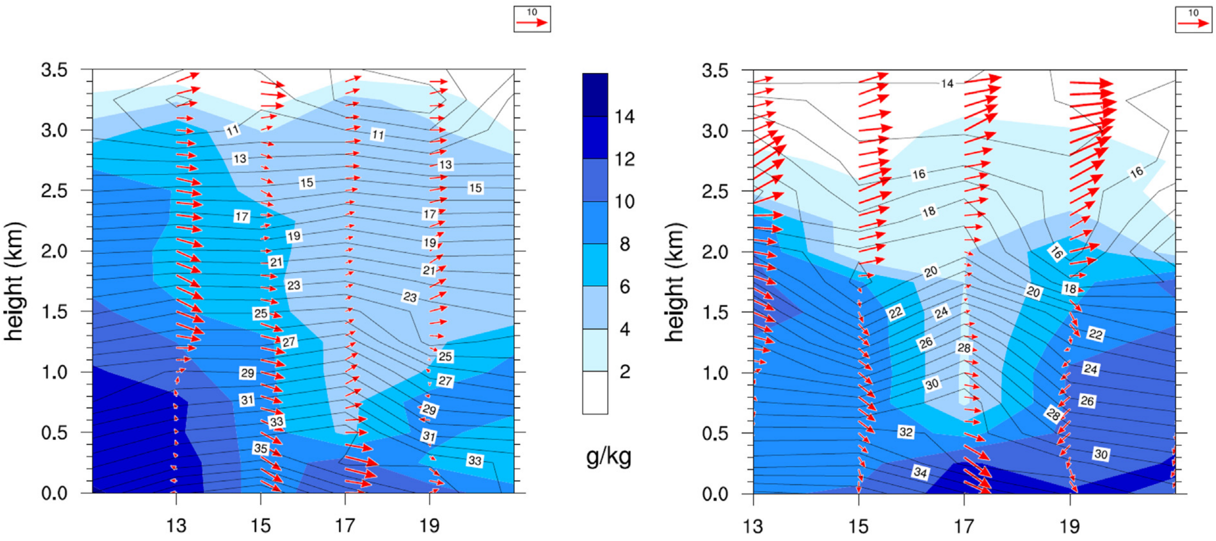

(b) WRF 16/8/2014

(d) WRF 8/8/2014

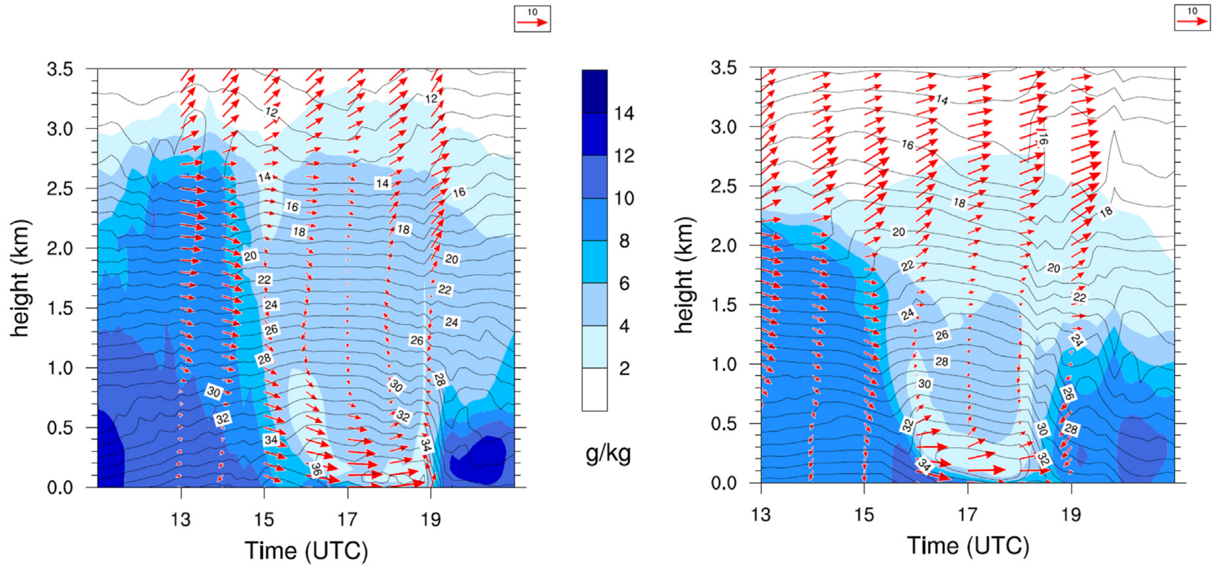

Fig. 10. Masada-Opera time evolution of horizontal wind (m/s, arrows), specific humidity (g/kg, shaded colors, with scale to the right of each panel), and temperature (^{0}C, contours) profiles from (a) radiosondes and (b) WRF model, 16 August 2014; from (c) radiosondes and (d) WRF model, 8 August 2014. Horizontal wind scale (in m/s) is shown at the upper-right corner of each panel. Zero height refers to the ground level of the measurements (Opera area, Fig. 1, −350 m ASL).

inversion layer has higher moisture associated with the MSB (as compared to 16 August, Fig. 11d); see Fig. 11b, where the moisture is located west to M up to ~1 km above the surface. This is in agreement with the surface SH increase on 8 August.

5. Discussion and conclusions

The MSB is one of the most central features of the DS valley summer climate. Two days with quite different near surface SH and temperature variations at the MSB arrival time into the DS valley were chosen. The MSB penetration into the DS valley has been studied for decades, however, those studies relied mostly on surface observations and coarse model simulations. Our study allowed for the first time the use of HR (both vertical and temporal) measurements and HR 3D modeling. These tools shed light on the dynamics responsible for the different outcomes observed at the surface of the DS valley following the MSB penetration.

The development of the MSB along with its inland penetration on both days was observed at surface stations extending from the coast up to top of the Judean Mountains and down to the DS valley. On 16 August, observations show that the MSB arrival was followed by a change in wind direction from NE to NW, a significant increase in the horizontal wind speed (up to ~10 m/s), development of a most significant downward vertical wind (−1 m/s), a sharp temperature increase (~1 °C), and also SH decrease (~2 g/kg). All these were observed from the surface up to ~1000 m AGL. A very sharp decrease in the IWV was measured by the radiometer. Decrease in surface SH and increase in surface temperature are frequent in the DS valley following the MSB arrival. Such a strong phenomenon as on 16 August was observed 4 times during August 2014 with similar synoptic conditions of the Persian Trough. As shown by Paperman (2017), in most days the surface SH decrease is not as pronounced and may even increase, as seen here on 8 August.

On the 8 August, the MSB arrival was also followed by high intensity horizontal wind speeds, but the wind direction changed from N to NW, vertical downward winds were observed but only below 400 m AGL, temperature decreased below 400 m AGL and increased above (400 -

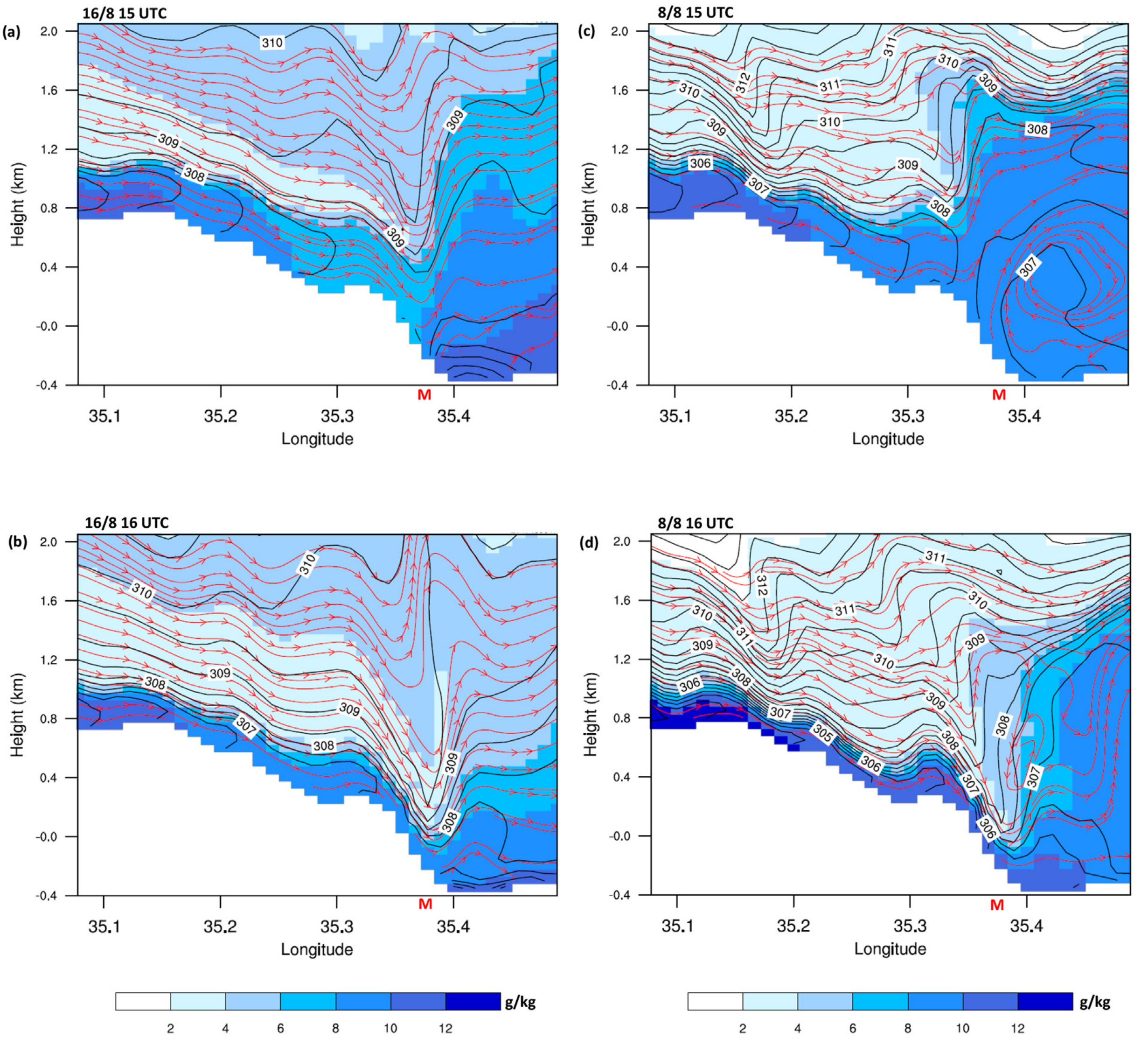

Fig. 11. WRF model W-E cross-sections for 2 chosen times (a) 1500 and (b) 1600 UTC on 16 August 2014; (c) 1500 and (d) 1600 UTC on 8 August 2014. Shaded colors represent specific humidity (g/kg, colour bar at bottom) black contours potential temperature (K) and red streamlines for UW flow. “M” at the horizontal axis indicates the location of the Opera measurements area. (For interpretation of the references to colour in this figure legend, the reader is referred to the web version of this article.)

Table 4
Hydraulic jump characteristics. *wmax* is the maximum vertical velocity, *Frcoast*, *Frridge* and *Frvalley* are the values of *Fr* at the Mediterranean Sea coast, at the top of the Judean Mountains and at the bottom of the DS valley along the cross section line perpendicular to the coast respectively.

Date (August 2014)	Depth (km)	*wmax* (m/s)	*Frcoast*	*Frridge*	*Frvalley*
8	1.2	0.9	0.41	1.02	1.63
16	1.2	1.6	0.19	1.05	1.83

1000 m AGL), SH increased below 400 m and decreased above. The IWV decrease was not as sharp as observed on the 16th. Table 5 summarizes the main features of both events.

Sensitivity simulations were run to determine the best model configuration for this study. This configuration was then employed for both days and results compared to the observations. Evaluation of temperatures, horizontal and vertical winds, SH and IWV all show reasonable agreement with observations. The simulations and the observations show similar dynamic behavior at the time of MSB penetration to the DS valley. Model simulations provided a 3D picture not available in observations.

Model cross sections showed that foehn wind developed with the MSB descent to the DS valley and a weakening of the opposing upward winds on the lee side. The foehn characteristics on both days were influenced by the synoptic and mesoscale conditions that affected the vertical structure of the lower troposphere (different heights of stable layers). While on 16 August the foehn reached the surface of the DS valley (under Persian Trough system, high stable layer), on the 8 August it did not (under High to the West system, low stable layer). These different vertical depths of the foehn contributed to different behaviors of the surface temperature and surface SH following MSB arrival. An additional factor responsible for the different behavior of the surface SH on these two days is the amount of moisture brought by the DS and MSB breezes (drier DS breeze and moister MSB on 8 August). The causes for the different SH and temperature behavior are schematically summarized in Fig. 12. Hydraulic jumps were identified on both days in the model simulations during these foehn events. The 8 August hydraulic jump was lower due to the more stable boundary layer resulting from lower inversion on this day. The different behavior of the IWV is associated with the different synoptic conditions too.

Table 5
Summary of main characteristics for each of the events.

Parameter/date	16 August 2014	8 August 2014
Change in surface SH (g/kg) with MSB arrival	−5	2
Change in surface temperature (°C) during MSB arrival	1.2	-2
Change in surface wind speed (m/s)	From 1 to 8	From 1 to 8
Change in surface wind direction	From NE to NW	From N to NW
Change in IWV (kg/m2) during MSB arrival	−17	−9
Change in SH along the profile	Decreased at all levels up to 3000 m	Increased below 400 m, decreased between 400 and 1000 m
Change in temperature along the profile	Increased below 1000 m	Decreased below 400 m, increased between 400 and 1000 m
Change in horizontal wind direction along the profile	From NE to NW at all levels up to 1000 m	From N to NW below 400 m
Change in horizontal wind speed along the profile	Increased at all levels up to 1000 m maximum of 11 m/s at 300 m	Increased at all levels up to 1000 m, maximum of 10 m/s at 200 m
Change in vertical wind speed along the profile	Downward wind at all levels up to at least 600 m with maximum of −1 m/s	Downward wind below 400 m with maximum of −1 m/s (model)
Cross section (model)	Downward vertical wind at all levels up to 2000 m, with maximum of −1 m/s, adiabatic descent from 1200 m up to −400 m below MSL	Downward vertical wind below 800 m MSL, adiabatic descent from 1000 m up to −400 below MSL
Synoptic conditions	Weak Persian Trough	High to the West
Time of MSB arrival (UTC)	1430	1530

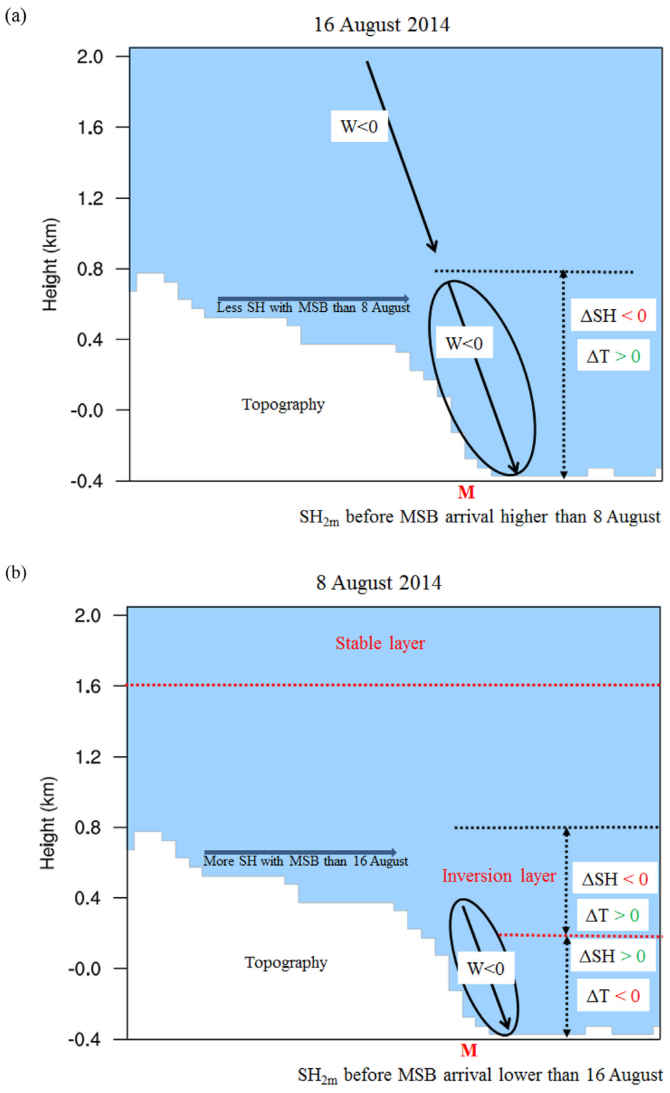

Fig. 12. A sketch map that summarizes the causes for the different SH and temperature behavior on (a) 16 August and (b) 8 August events.

It should be noted that the present study cannot quantitatively analyze the contributions of the different physical factors and their synergies to the observed phenomena. A Factor Separation (Stein and Alpert, 1993; Alpert and Sholokhman, 2011) study in which some physical factors are turned on/off in the model simulations to evaluate the effect of each of them and of their synergies is in preparation.

As stated in Section 4, our model-to-observations comparisons are aimed to provide confidence in the model to analyze the MSB 3D dynamics. Clearly, the model 1.1 km horizontal interval cannot capture some of the very small-scale features like the Masada hill, located in the immediate proximity of the measurements (Opera area, Fig. 1) that modify in particular the 3D-wind field. Model temperature and moisture biases were observed and further analysis (not shown here) reveals the limitations of the relatively coarse global analyses used for atmospheric and soil IC/BC. Spatial resolution, surface-layer/PBL crude parameterizations, and coarse IC/BC from global analyses are well known *meso*scale-modeling limitations. In the case of complex topography and sub-kilometer scale heterogeneities, as in the present case of the DS valley, Large Eddy Simulations (LES) could be considered to improve model skill (Arnold et al., 2012). In spite of all these, the model reproduced the main features of the two different events reasonably well. In addition, it provided valuable dynamical information not found in the observations (such as the cross sections discussed above) but absolutely required to explain the differences. Moreover, our simulations suggest the feasibility of HR forecasts of the foehn and sudden changes in temperature, SH and wind in the DS valley 24 h in advance. Such forecasts can be very valuable for the population in the area, in particular as they have implications to forecasts of contaminants in the area.

Even though the present research focuses on two case studies it presents a general methodology that sheds light onto the factors responsible for the variable 3D behavior observed at the time of MSB penetration and foehn/hydraulic-jump developments. Similar model and observations analyses may be extended to other cases in order to assess the dynamical factors responsible for the various observed outcomes.

Supplementary data to this article can be found online at https://doi.org/10.1016/j.atmosres.2019.06.012.

Acknowledgements

The German Helmholtz Association is gratefully acknowledged for (partly) funding this project within the Virtual Institute DESERVE (Dead Sea Research Venue) under contract number VH-VI-527. Special thanks to our German partners Jutta Metzger and Ulli Corsmeier for much help with the data and useful comments. Dr. Yehuda Alexander and Dr. David Avisar are thanked for reviewing the manuscript prior to submission.

We wish to thank the Israeli Meteorological Service (IMS) for providing ECMWF data.

References

Alpert, P., 1988. The combined use of three different approaches to obtain the best estimate of meso-β surface winds over complex terrain. Bound. Layer Meteorol. 45, 291–305.

Alpert, P., Eppel, A., 1985. A proposed index for mesoscale activity. J. Clim. Appl. Meteorol. 24, 472–480.

Alpert, P., Neumann, J., 1984. On the enhanced smoothing over topography in some mesometeorological models. Bound.-Layer Meteorol. 30, 293–312.

Alpert, P., Rabinovich-Hadar, M., 2003. Pre- and post- frontal lines - a meso gamma scale analysis over South Israel. J. Atmos. Sci. 60, 2994–3008.

Alpert, P., Sholokhman, T., 2011. In: Alpert, P., Sholokhman, T. (Eds.), Factor Separation in the Atmosphere, Applications and Future Prospects. Cambridge University Press, pp. 274.

Alpert, P., Cohen, A., Neumann, J., Doron, E., 1982. A model simulation of the summer circulation from the Eastern Mediterranean past Lake Kinneret in the Jordan Valley. Mon. Weather Rev. 110, 994–1006.

Alpert, P., Abramski, R., Neeman, B.U., 1990. The prevailing summer system in Israel - subtropical High not Persian Trough. Isr. J. Earth Sci. 39, 93–102.

Alpert, P., Osetinsky, I., Ziv, B., Shafir, H., 2004. Semi-objective classification for daily synoptic systems: application to the eastern Mediterranean climate change. Int. J. Climatol. 24 (8), 1001–1011.

Arnold, D., Morton, D., Schicker, I., Seibert, P., Rotach, M., Horvath, K., Dudhia, J., Satomura, T., Müller, M., Zängl, G., Takemi, T., Serafin, S., Schmidli, J., Schneider, S., Feb 2012. 2012. Highresolution modeling in complex terrain. Report on the HiRCoT 2012 Workshop, Vienna. pp. 21–23.

Ashbel, D., 1939. The influence of the Dead Sea on the climate of its neighbourhood. Quart. J. R. Met. Soc. 65, 185–194.

Atkinson, B.W., 1981. Mesoscale Atmospheric Circulation. Academic Press, pp. 495.

Berkovic, S., 2016. Synoptic classes as a predictor of hourly surface wind regimes: the case of the central and southern Israeli coastal plains. J. Appl. Meteorol. Climatol. 55, 1533–1547. https://doi.org/10.1175/JAMC-D-16-0093.1.

Bitan, A., 1977. The influence of the special shape of the Dead Sea and its environment on the local wind system. Arch. for Meteorology. Geophys. Bioclimatol. B 24, 283–301.

Browning, K.A., Wexler, R., 1968. The determination of kinematic properties of a wind field using Doppler radar. J. Appl. Meteorol. 7, 105–113.

Chemel, C., Sokhi, R.S., 2012. The response of London's urban heat island to a marine air intrusion in an easterly wind regime. Bound.-Layer Meteorol. 144, 65–81. https://doi.org/10.1007/s10546-012-9705-x.

Crewell, S., Löhnert, U., 2003. Accuracy of cloud liquid water path from ground-based microwave radiometry. Part II. Sensor accuracy and synergy. Radio Sci. 38, 8042. https://doi.org/10.1029/2002RS002634.

Crosman, E.T., Horel, J.D., 2010. Sea and lake breezes: a review of numerical studies. Bound.-Layer Meteorol. 137, 1–29. https://doi.org/10.1007/s10546-010-9517-9.

Dayan, U., Lifshitz-Goldreich, B., Pick, K., 2002. Spatial and structural variation of the atmospheric boundary layer during summer in Israel-Profiler and rawinsonde measurements. J. Appl. Meteorol. 41, 447–457.

Doron, E., Neumann, J., 1977. Land and mountain breezes with special attention to Israel's Mediterranean coastal plain. Isr. Meteor. Res. Pap. 1, 109–122.

Duran, D.R., 1990. Mountain waves and downslope winds. In: Blumen, William (Ed.), Atmospheric Process over Complex Terrain. American Meteorological Society, Boston, pp. 59–81.

Grell, G.A., 1993. Prognostic evaluation of assumptions used by cumulus parameterizations. Mon. Weather Rev. 121, 764–787.

Grell, G.A., Devenyi, D., 2002. A generalized approach to parameterizing convection combining ensemble and data assimilation techniques. Geophys. Res. Lett. 29, 1693.

Hari Prasad, K.B.R.R., Srinivas, S.D., Narayana Rao, T., Naidu, C.V., Baskaran, R., 2017. Performance of WRF in simulating terrain induced flows and atmospheric boundary layer characteristics over the tropical station Gadanki. Atmos. Res. https://doi.org/10.1016/j.atmosres.2016.10.020.

Hong, S.-Y., Noh, Y., Dudhia, J., 2006. A new vertical diffusion package with an explicit treatment of entrainment processes. Mon. Wea. Rev. 134, 2318–2341. https://doi.org/10.1175/MWR3199.1.

Hu, X., Nielsen-Gammon, J.W., Zhang, F., 2010. Evaluation of three planetary boundary layer schemes in the WRF model. J. Appl. Meteorol. Climatol. 49, 1831–1844.

Iacono, M.J., Delamere, J.S., Mlawer, E.J., Shephard, M.W., Clough, S.A., Collins, W.D., 2008. Radiative forcing by long–lived greenhouse gases: Calculations with the AER radiative transfer models. J. Geophys. Res. 113 (D13103).

Janjic, Z.I., 1994. The step–mountain eta coordinate model: further developments of the convection, viscous sublayer, and turbulence closure schemes. Mon. Weather Rev. 122, 927–945.

Janjic, Z.I., 1996. The surface layer in the NCEP Eta model. In: Eleventh Conference on Numerical Weather Prediction, Norfolk, VA, 19–23 August 1996. Amer Meteor Soc, Boston, MA, pp. 354–355.

Janjic, Z.I., 2002. Nonsingular implementation of the Mellor-Yamada Level 2.5 Scheme in the NCEP Meso model. NCEP Office Note 437, 61.

Kalthoff, N., Adler, B., Wieser, A., Kohler, M., Träumner, K., Handwerker, J., Corsmeier, U., Khodayar, S., Lambert, D., Kopmann, A., Kunka, N., Dick, G., Ramatschi, M., Wickert, J., Kottmeier, C., 2013. Kitcube—a mobile observation platform for convection studies deployed during HyMeX. Meteorol. Z. 22 (6), 633–647.

Kishcha, P., Starobinets, B., Savir, A., Alpert, P., Kaplan, M., 2017. Foehn-induced effects on dust pollution, frontal clouds and solar radiation in the Dead Sea valley. Meteorog. Atmos. Phys. 1–15.

Klai'c, Z.B., Pasari'c, Z., Tudor, M., 2009. On the interplay between sea-land breezes and Etesian winds over the Adriatic. J. Mar. Syst. 78 (Supplement), S101–S118. https://doi.org/10.1016/j.jmarsys.2009.01.016.

Lensky, I.M., Dayan, U., 2012. Continuous detection and characterization of the Sea Breeze in clear sky conditions using Meteosat second generation. Atmos. Chem. Phys. 12, 6505–6513.

Levin, Z., Gershon, H., Ganor, E., 2005. Vertical distribution and chemical properties of haze particles in the Dead Sea valley. Atmos. Environ. 39, 4937–4945.

Lin, Y.-L., 2007. Mesoscale Dynamics. Cambridge University Press, pp. 215–220.

Lin, Y.-L., Farley, R.D., Orville, H.D., 1983. Bulk parameterization of the snow field in a cloud model. J. Climate Appl. Met. 22, 1065–1092.

Löhnert, U., Crewell, S., 2003. Accuracy of cloud liquid water path from ground-based microwave radiometry. Part I. Dependency on cloud model statistics. Radio Sci. 38, 8041. https://doi.org/10.1029/2002RS002654.

Miao, Y., Hu, X.-M., Liu, S., Qian, T., Xue, M., Zheng, Y., Wang, S., 2015. Seasonal variation of local atmospheric circulations and boundary layer structure in the Beijing-Tianjin-Hebei region and implications for air quality. J. Adv. Model. Earth Syst. 7 (1), 1–25 (DOI: 5 10.1002/2015MS000522).

Miller, S.T.K., Keim, B.D., Talbot, R.W., Mao, H., 2003. Sea breeze: structure, forecasting, and impacts. Rev. Geophys. 41 (3), 1–31.

Naor, R., Potchter, O., Shafir, H., Alpert, P., 2017. An observational study of the summer Mediterranean Sea-breeze-front penetration into the complex topography of the Jordan-Rift-Valley. Theor. Appl. Climatol. 127 (1–2), 275–284. https://doi.org/10.1007/s00704-015-1635-3.

Nkemdirim, L.C., Leggat, K., 1978. The effect of chinook weather on urban heat islands and air pollution. Water, Soil, Air Poll. 9, 5347.

Norte, F., 2015. Understanding and Forecasting Zonda Wind (Andean Foehn) in Argentina: A Review. Atmospheric and Climate Sciences 5, 163–193. https://doi.org/10.4236/acs.2015.53012.

Papanastasiou, D.K., Melas, F., Lissaridis, I., 2010. Study of wind field under sea breeze conditions; an application of WRF model. Atmos. Res. 98 (1), 102–117.

Paperman, J., 2017. A-3D Characterization of the Summer Daily Wind Regime in the Dead Sea. M.Sc Thesis. Tel Aviv University.

Peace, M., Mattner, T., Mills, G., Kepert, J., McCaw, L., 2015. Fire-modified meteorology in a coupled fire–atmosphere model. J. Appl. Meteorol. Climatol. 54, 704–720. https://doi.org/10.1175/JAMC-D-14-0063.1.

Richner, H., Hachler, P., 2013. Understanding and Forecasting Alpine Foehn. In: Chow, F.K., De Wekker, S.F.J., Snyder, B.J. (Eds.), Mountain Weather Research and Forecasting (Chapter 4). Springer Atmospheric Sciences, pp. 219–260. https://doi.org/10.1007/978-94-007-4098-3_4.

Robinson, F.J., Patterson, M.-D., Sherwood, S.C., 2013. A numerical modeling study of the propagation of idealized sea-breeze density currents. J. Atmos. Sci. 70, 653–668. https://doi.org/10.1175/JAS-D-12-0113.1.

Salvador, N., Reis Jr., N.C., Santos, J.M., Toledo de Alburquerque, T., Loriato, A.G., Delbarre, H., Augustin, P., Sokolov, A., Moreira, D.M., 2016. Evaluation of weather research and forecasting model parameterizations under sea-breeze conditions in a North Sea coastal environment. J. Meteor. Res. 30, 998–1018. https://doi.org/10.1007/s13351-016-6019-9.

Segal, M., Mahrer, Y., Pielke, R.A., 1983. A study of meteorological patterns associated with a lake confined by mountains—the Dead Sea case. Q. J. R. Meteorol. Soc. 109, 549–564.

Sever, L., Alpert, P., Lyapustin, A., Wang, Y., Chudnovsky, A., 2017. An example of aerosol pattern variability over bright surface using high resolution MODIS MAIAC: the eastern and western areas of the Dead Sea and environs. Atmos. Environ. 165, 359–369.

Shafir, H., Alpert, P., 2011. Regional and local climatic effects on the DeadSea evaporation. Clim. Chang. 105, 455–468. https://doi.org/10.1007/s10584- 010-9892-8.

Simpson, J.E., 1994. Sea Breeze and Local Winds. Cambridge University Press, pp. 228.

Simpson, J.E., Mansfield, D.A., Milford, J.R., 1977. Inland penetration of sea-breeze fronts. Q. J. R. Meteorol. Soc. 103, 47–76.

Skamarock, W., Klemo, K., Dudhia, J., Gill, D., Barker, D., Duda, M., Huang, X., Wang, W., Powera, J., 2008. A description of the Advanced Research WRF Version. pp. 3.

Skibin, D., Hod, A., 1979. Subjective analysis of mesoscale flow patterns in Northern Israel. J. Appl. Meteorol. 18, 329–338.

Smagorinsky, J., 1963. General circulation experiments with the primitive equations. Mon. Weather Rev. 91, 99–164.

Soler, M., Udina, M., Ferreres, W., 2014. Observational and numerical simulation study of a sequence of eight atmospheric density currents in Northern Spain. Bound.-Layer Meteorol. 153, 1–22.

Stein, U., Alpert, P., 1993. Factor separation in numerical simulations. J. Atmos.Sci. 50, 2107–2115.

Takane, Y., Kusaka, H., 2011. Formation mechanisms of the extreme high surface air temperature of 40.9°C observed in the Tokyo metropolitan area: considerations of dynamic foehn and foehnlike wind. J. Appl. Meteorol. Climatol. 50, 1827–1841. https://doi.org/10.1175/JAMC-D-10-05032.1.

Tewari, M., Chen, F., Wang, W., Dudhia, J., LeMone, M.A., Mitchell, K., Ek, M., Gayno, G., Wegiel, J., Cuenca, R.H., 2004. Implementation and verification of the unified NOAH land surface model in the WRF model. In: 20th Conference on weAther Analysis and Forecasting/16th Conference on Numerical Weather Prediction, pp. 11–15.

Träumner, K., Kottmeier, C., Corsmeier, U., Wieser, A., 2011. Convective boundary-layer entrainment: short review and progress using Doppler lidar. Bound.-Layer Meteorol. 141, 369–391.

Udina, M., Soler, M.R., Viana, S., Yagüe, C., 2013. Model simulation of gravity waves triggered by a density current. Q. J. R. Meteorol. Soc. 139, 701–714. https://doi.org/10.1002/qj.2004.

Vüllers, J., Mayr, G.J., Corsmeier, U., Kottmeier, C., 2018. Characteristics and evolution of diurnal foehn events in the Dead Sea valley. Atmos. Chem. Phys. 18, 18169–18186. https://doi.org/10.5194/acp-18-18169-2018.

Zhang, H.L., Pu, Z.X., Zhang, X.B., 2013. Examination of errors in near-surface temperature and wind from WRF numerical simulations in regions of complex terrain. Wea. Forecasting 28 (3), 893–914. https://doi.org/10.1175/Waf-D-12-00109.1.

Ziv, B., Saaroni, H., Alpert, P., 2004. The factors governing the summer regime of the eastern Mediterranean. Int. J. Climatol. 24, 1859–1871.